displaying a much stronger temperature dependence, which is suggestive of unusual low-energy vibrational modes in addition to the normal acoustic phonons.

A first attempt to model this unusual behaviour, taking into account the presence of harmonic Einstein-oscillators, failed to describe the 'dip' in the data at low temperatures. The elastic data can, however, be described by considering the elastic response of a two-level system (TLS) with level-spacing Δ. We can calculate the TLS-contribution to the elastic response, $c = \partial^2 F/\partial\epsilon^2$, with $F = -N_A k_B T \ln(1 + e^{-\Delta/T})$ the Helmholtz free energy of a TLS, and assuming that the vibrational level spacing, Δ, depends linearly on the strain, ϵ, that is, $\Delta = \Delta_0 + A\epsilon$, with A a coupling constant. As illustrated in Fig. 2, both the c_{11} and c_{44} modulus can be modelled reasonably well by adding two TLSs, with level spacings of 50 and 200 K. The dashed line in Fig. 2 represents the 'background' contribution, which is estimated from the Varshni-fit for the unfilled skutterudite $CoSb_3$.

As the TLS approach quite effectively models the RUS data, whereas the Einstein modes fail, we investigated whether the specific heat, modelled above with two Einstein oscillators, could be described using two-level systems. We found that the data can indeed by modelled using two TLSs, with level spacing of 70 and 200 K. Both approaches seem to be indistinguishable in the experimental temperature range (2–45 K).

Inelastic neutron scattering can provide a quantitative measure of the vibrational density of states of a solid as a function of energy. Although quantitative interpretation of the data from a multi-element solid is only possible with a detailed model of the lattice dynamics, qualitative information can be extracted by comparing the measured vibrational spectrum to that of a suitable reference compound. Figure 3 shows the difference in the vibrational spectrum between $LaFe_4Sb_{12}$ and $CeFe_4Sb_{12}$ obtained from neutron-scattering measurements made at the ISIS facility of the Rutherford Appleton Laboratory, UK. The scattering cross-section for Ce is much less than for La, and hence this difference spectrum tends to emphasize the features of the vibrational spectrum associated with La. The neutron data show a well defined peak at 7 meV (80 K) and a somewhat broader feature at 15 meV (175 K). These energies are in good agreement with the values obtained from the heat capacity and RUS measurements. Truly localized modes should appear as delta functions in the vibrational density of states, but hybridization with acoustic phonons will tend to broaden the peaks.

The neutron data provide strong evidence that both local modes have to be associated with the presence of the La ion, suggesting that there are two distinct eigenmodes associated with the rattling of the ion. The structure of the material makes two different La motions likely. The rattling La ion can move towards one of its nearest neighbour Sb atoms, or it can move towards a 'void'. One would expect that if the La ion moves toward a 'void', its vibrations would have a lower frequency and be more localized than if it moved towards a nearest-neighbour Sb. The neutron results are consistent with this picture. The peak at 15 meV is considerably broader than the 7-meV peak, indicating that hybridization with other modes is stronger. This implies that the 15-meV mode is less localized than the 7-meV mode. Hybridization might also be the reason why Einstein oscillators cannot perfectly describe the local modes. Higher levels of the harmonic well that are hybridized with extended phonons will lose their 'local' character, effectively reducing the harmonic oscillator to a simple TLS.

To the best of our knowledge, the only metallic compound with a well-defined local phonon mode is $Al_{10}V$, which has[13] an Einstein temperature of 22 K. Compared to $Al_{10}V$, however, filled skutterudites have a number of advantages. Whereas $Al_{10}V$ poses formidable materials difficulties, filled skutterudites can be made single-phase and single crystals can be grown. Moreover, by controlling the filling of the rare-earth site, the carrier concentration and thus the transport properties of the material could be modified. Furthermore, various magnetic ions could be placed on the rare-earth site, and the effects of local phonon modes on a wide variety of ground states could be studied. □

Received 2 June; accepted 6 August 1998.

1. Jeitschko, W. & Braun, D. J. $LaFe_4P_{12}$ with filled $CoAs_3$-type structure and isotypic lanthanoid-transition metal polyphosphides. *Acta Crystallogr. B* **33,** 3401–3405 (1977).
2. Braun, D. J. & Jeitschko, W. Preparation and structural investigations of antimonides with the $LaFe_4P_{12}$ structure. *J. Less-Common Met.* **72,** 147–156 (1988).
3. Morelli, D. M. & Meisner, G. P. Low temperature properties of the filled skutterudite $CeFe_4Sb_{12}$. *J. Appl. Phys.* **77,** 3777–3781 (1995).
4. Sales, B. C. *et al*. Filled skutterudite antimonides: electron crystals and phonon glasses. *Phys. Rev. B* **56,** 15081–15089 (1997).
5. Sales, B. C., Mandrus, D. & Williams, R. K. Filled skutterudite antimonides: a new class of thermoelectric materials. *Science* **272,** 1325–1328 (1996).
6. Grandjean, F. *et al*. Some physical properties of $LaFe_4P_{12}$ type compounds. *J. Phys. Chem. Solids* **45,** 877–886 (1984).
7. Meisner, G. P. Superconductivity in $LaFe_4P_{12}$. *Physica B* **108,** 763–764 (1981).
8. Meisner, G. P. *et al*. UFe_4P_{12} and $CeFe_4P_{12}$: nonmetallic isotypes of superconducting $LaFe_4P_{12}$. *J. Appl. Phys.* **57,** 3073–3075 (1985).
9. Danebrock, M. E., Evers, C. B. H. & Jeitschko, W. Magnetic properties of alkaline earth and lanthanoid iron antimonides with the $LaFe_4P_{12}$ structure. *J. Phys. Chem. Solids* **57,** 381–387 (1996).
10. Feldman, J. L. & Singh, D. J. Lattice dynamics of skutterudites: first principles and model calculations for $CoSb_3$. *Phys. Rev. B* **53,** 6273–6282 (1996). Erratum **54,** 712 (1996).
11. Migliori, A. *et al.* Resonant ultrasound spectroscopic techniques for measurements of the elastic moduli of solids. *Physica B* **183,** 1–24 (1993).
12. Varshni, P. Temperature dependence of the elastic constants. *Phys. Rev. B* **2,** 3952–3958 (1970).
13. Caplin, D., Grüner, G. & Dunlop, J. B. $Al_{10}V$: An Einstein solid. *Phys. Rev. Lett.* **30,** 1138–1140 (1973).

Acknowledgements. We thank J. Feldman and R. Leisure for discussions, and A. Migliori and T. Darling for assistance with the RUS measurements. This work was supported by the Division of Materials Sciences, US Department of Energy, a Cooperative Research and Development Agreement with Marlow Industries, and the NSF.

Correspondence and requests for materials should be addressed to B.C.S. (e-mail: vb4@ornl.gov).

Synthesis of individual single-walled carbon nanotubes on patterned silicon wafers

Jing Kong*†, Hyongsok T. Soh†‡, Alan M. Cassell*, Calvin F. Quate‡ & Hongjie Dai*

** Department of Chemistry, ‡ Department of Electrical Engineering, Stanford University, Stanford, California 94305, USA*
† These authors contributed equally to this work

Recent progress[1–3] in the synthesis of high-quality single-walled carbon nanotubes[4] (SWNTs) has enabled the measurement of their physical and materials properties[5–8]. The idea that nanotubes might be integrated with conventional microstructures to obtain new types of nanoscale devices, however, requires an ability to synthesize, isolate, manipulate and connect individual nanotubes. Here we describe a strategy for making high-quality individual SWNTs on silicon wafers patterned with micrometre-scale islands of catalytic material. We synthesize SWNTs by chemical vapour deposition of methane on the patterned substrates. Many of the synthesized nanotubes are perfect, individual SWNTs with diameters of 1–3 nm and lengths of up to tens of micrometres. The nanotubes are rooted in the islands, and are easily located, characterized and manipulated with the scanning electron microscope and atomic force microscope. Some of the SWNTs bridge two metallic islands, offering the prospect of using this approach to develop ultrafine electrical interconnects and other devices.

Our synthesis begins with the patterning of catalytic islands on silicon substrates. A schematic of the process flow is shown in Fig. 1. For regularly spaced catalytic islands on the silicon surface, the essential fabrication steps are: electron-beam lithography, deposition of $Fe(NO_3)_3{\cdot}9H_2O$, $MoO_2(acac)_2$ and alumina nanoparticles in the liquid phase and lift-off (Fig. 1). The square islands are spaced at a 10-μm pitch, and the size of islands is 3 μm or 5 μm. For

chemical-vapour-deposition (CVD) growth, the patterned substrate is first heated in a tube furnace to reach 1,000 °C in an argon atmosphere. The argon flow is replaced by methane (99.99%) at a flow rate of 1,000 to 6,000 $cm^3 min^{-1}$. The methane flow is maintained for 10 min at 1,000 °C before being replaced by argon until the furnace cools to room temperature.

We have characterized our samples with a Hitachi field emission scanning electron microscope (SEM). In Fig. 2a, b, we show two SEM micrographs recorded on the 5-μm islands. The dark, square-shaped areas are the hill-like islands. Several important features are noted in the SEM micrographs. First, we observe line-like structures coming off the islands. Some of the lines are bridging adjacent islands. Second, the lines appear dark over a brighter background of the substrate, and some of the end points of the lines can be identified. Third, the lines appear relatively straight and extend up to more than 10 μm. These SEM results indicate that carbon nanotubes may have been synthesized from the islands. We show later that a large fraction of the nanotubes are individual SWNTs. The sole reason that we can observe individual SWNTs by SEM is because of the electrical connections existing between nanotubes and islands which render them as dark lines in the SEM images.

Further sample characterization was carried out using an atomic force microscope (AFM). An AFM image recorded on 5-μm islands,

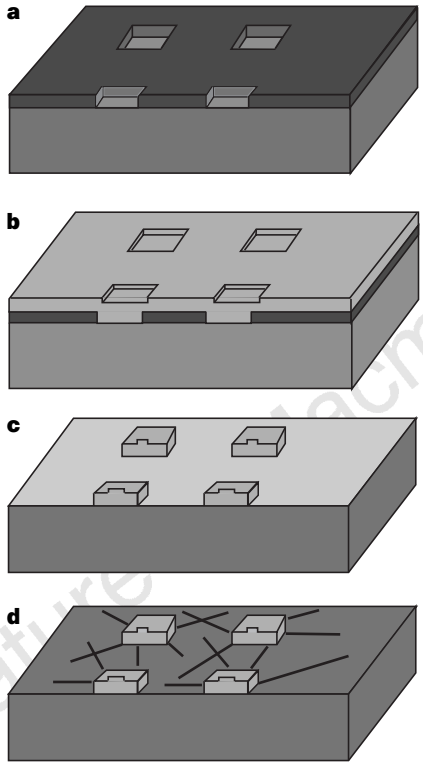

Figure 1 Schematic of process flow. **a–c**, Process flow for fabricating catalytic islands on silicon substrates used in CVD nanotube growth (**d**). **a**, Electron beam lithography was used to fabricate square holes in a polymethylmethacrylate (PMMA) film on silicon. We used p-type Si(100) substrate (resistivity 10 Ω cm) without removing the native oxide. The 0.25-μm-thick PMMA film was obtained by spin coating (at 4,000 r.p.m.) the silicon substrate with a 5% PMMA (relative molecular mass, 495K) chlorobenzene solution, followed by baking at 170 °C for 2 h. Electron-beam patterning was done using a Hitachi HL700F machine operated at 30 kV; exposure dosage was 500 μC cm^{-2}. The exposed PMMA was removed with a methyl isobutyl ketone (MIBK) and isopropyl alcohol (3:1) solution. **b**, 0.05 mmol $Fe(NO_3)_3{\cdot}9H_2O$, 0.015 mmol of MoO_2 $(acac)_2$ and 15 mg alumina nanoparticles (Degussa, aluminum oxide C; average particle size, 14 nm) was added to 15 ml methanol. The mixture was stirred for 24 h and sonicated for 1 h to afford a 0.05 mmol/15 mg/15 ml $Fe(NO_3)_3{\cdot}9H_2O$/alumina/methanol suspension. A drop of the suspension was deposited onto the patterned PMMA substrate. After solvent vaporization at room temperature, the substrate was heated at 170 °C for 5 min. **c**, Lift-off of PMMA in 1,2-dichloroethane leads to the final substrate containing catalyst islands. **d**, CVD of methane at 1,000 °C produces SWNTs off the islands (see other figures and text).

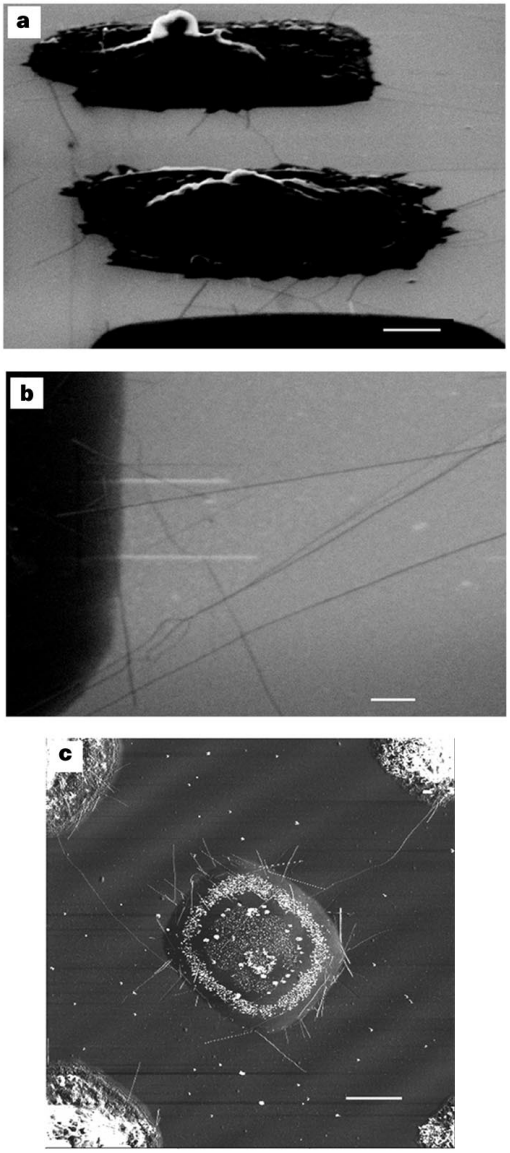

Figure 2 Nanotubes grown on a catalyst-patterned substrate. **a**, Scanning electron microscope (SEM) image that shows line-like structures (nanotubes; see text) extending off the patterned 5-μm islands on silicon after methane CVD. The sample was tilted at a 65° angle relative to the incident electron beam (25 kV). The dark protrusions on the surface are the square islands. Nanotubes appear as dark lines because they have electrical connections with the metallic islands. The brighter background is due to the electron charging effect of the silicon oxide substrate. Note that some of the nanotubes are bridging islands. Scale bar: 1 μm. **b**, A high-magnification (scale bar: 300 nm) SEM image recorded with the same sample as in **a**. Clearly, nanotubes are connected to the island (dark region) and most of the nanotubes appear extremely straight at the micrometre scale. **c**, Typical large-scale (scale bar: 2 μm) phase image recorded by tapping mode AFM, showing carbon nanotubes grown from the patterned islands and bridging between islands.

shown in Fig. 2c, reveals similar line-like structures. Extensive topographic imaging by tapping mode AFM found that the line-like structures are indeed synthesized nanotubes with higher topography than the Si substrate. The topography image in Fig. 3a shows that all nanotubes are connected with the islands. Several nanotubes have one end resting in between islands, whereas nanotubes that bridge islands have both ends buried in the two opposing islands. From height measurements, we determined that the diameters of the nanotubes in Fig. 3a range from 0.8 nm to 3.0 nm, which strongly suggests that individual SWNTs were synthesized off the islands. In Fig. 3b, we show an SWNT (2.2 nm in diameter) bridging two diagonal islands. We found that lowering the concentrations of $Fe(NO_3)_3{\cdot}9H_2O$ and alumina led to the formation of islands shaped like doughnuts. Figure 3c, d shows AFM images recorded on 3-μm doughnut-shaped islands. The average diameter of nanotubes in Fig. 3c is 1.6 nm, and the length of nanotubes extends up to more than 20 μm. To illustrate further the high quality of the synthesized individual SWNTs, we show in Fig. 3d a higher-magnification AFM topography image. Note that nanotubes on the line-cut (Fig. 3d) have diameters that range from 1.2 to 2.7 nm (Fig. 3e).

We emphasize several important features of the nanotube materials synthesized by this approach. First, about 90% of the nanotubes, having diameters in the range of 1–3 nm, are individual SWNTs. SWNTs with diameters ranging from ~1 up to 5 nm have been observed previously in materials synthesized by arc discharge[9,10]. Second, we found that the SWNTs are remarkably straight, considering their extreme aspect ratios of up to 10^4. So far we have not observed nanotubes with frequent kinks along their length: only smooth curving exists. These SWNTs must be nearly free of topological defects arising from pentagons and heptagons along the side walls. Third, our synthetic method is very simple and can be scaled up on full-size silicon wafers. Finally, our synthesis directly fabricates high-quality individual SWNT devices needed for fundamental and practical purposes[11]. Essentially, the frequently observed nanotube bridges crosslink the micrometre-scale islands

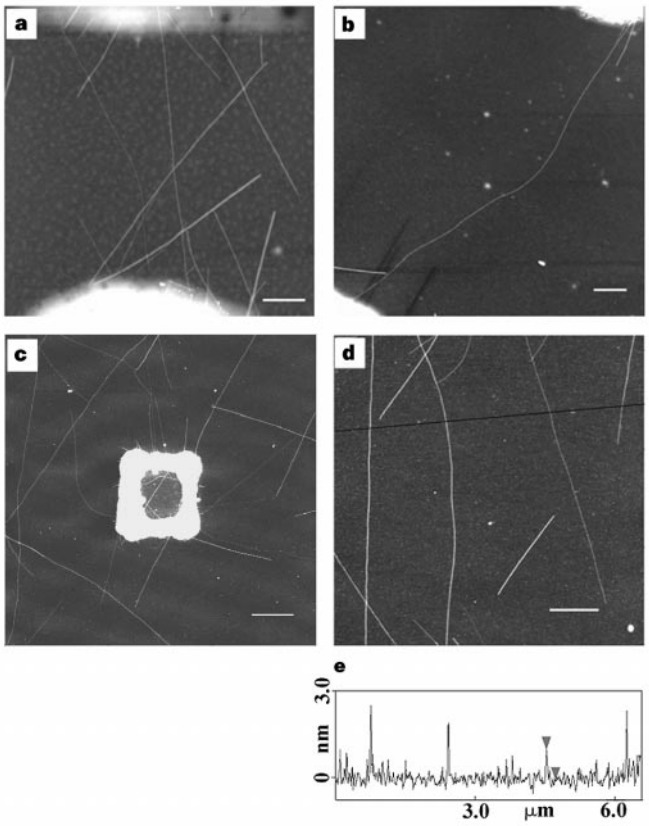

Figure 3 Topography images of individual SWNTs recorded by tapping mode AFM. Commercial silicon cantilevers with ~100 N m^{-1} stiffness and ~250 kHz resonance frequency were used. **a**, Image recorded on the 5-μm islands showing individual SWNTs synthesized off the islands. The bright regions at the top and bottom of the image are the edges of two adjacent islands. Nanotubes in this image have diameters between 0.9 and 3 nm (scale bar: 500 nm). **b**, Image recorded with the 5-μm islands showing a 2-nm diameter individual SWNT bridging two islands. The bright regions at the upper right and lower-left corners of the image are the edges of two diagonal islands (scale bar: 500 nm). **c**, Data recorded with a 3-μm doughnut-shaped island showing long individual SWNTs growing off doughnut-shaped islands and making a network. In the image, several nanotubes are from adjacent islands, the average nanotube diameter is 1.6 nm, and the nanotubes are up to 20 μm long (scale bar: 2 μm). **d**, Image of individual SWNTs showing that each nanotube appears uniform in both width and height (scale bar: 1 μm). We note a mysterious nanotube in this image that has both ends unconnected with any island, a phenomenon that occurs rarely. **e**, Topographic height measurements for nanotubes on the line-cut (black line) in **d**. The measured diameters of the four individual SWNTs are 2.7, 1.8, 1.2 and 1.8 nm, respectively.

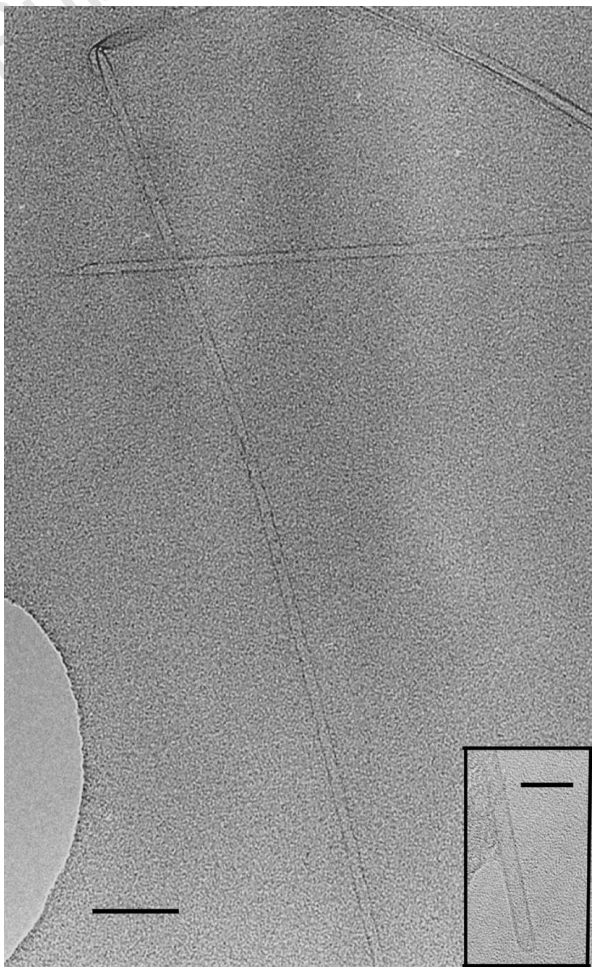

Figure 4 A transmission electron microscope (TEM) image (scale bar: 50 nm) of an individual SWNT synthesized on supported catalysts by the methane CVD approach. The image background is due to the holey carbon film on the TEM grid. The inset (scale bar: 10 nm) shows a typical closed particle-free end of an individual nanotube. We note that a small fraction of the SWNTs are in bundled form (for detailed results, see ref. 17). For TEM sample preparation, we suspended 10 mg of the synthesized material in methanol by sonication for 15 min, and then put a few drops of the suspension onto the TEM grid.

into a macroscopic electrical network. Thus, electrical connections from the macroscopic scale to individual SWNTs can now be easily made via the micrometre-scale islands. Using this approach, we have designed and fabricated individual SWNT electrical circuits by direct CVD syntheses on insulating SiO_2 substrates with the patterned catalyst islands connected to macroscopic metal electrodes (see Supplementary Information). By mechanical manipulation of nanotube bridges using contact mode AFM[12], we have obtained evidence of strong mechanical fixation of nanotubes to the islands. Further, we have measured the lateral forces needed to break individual SWNTs and estimated the tensile strength of SWNTs (of the order of 200 GPa; see Supplementary Information).

We have chosen methane for carbon feedstock in our CVD synthesis because methane is the most kinetically stable hydrocarbon at elevated temperatures. Previously, extensive work has been done using methane in catalysed CVD synthesis of carbon fibres at temperatures up to 1,100 °C (refs 13–16). At 1,000 °C, the catalytic decomposition of methane by our catalyst dominates over self-pyrolysis, at least within a timescale of 10 min. This is evident from our observation that no obvious amorphous carbon coating exists on the side walls of the nanotubes. However, an amorphous carbon coating can build up over time. Previous work on micrometre-scale carbon-fibre synthesis showed that as the reaction is allowed to take place for hours, methane pyrolysis at ~1,000 °C leads to an appreciable thickness of carbon coating over a nanotube core[13–16]. By limiting our CVD synthesis to 10 min and using a relatively high flow rate, we are able to avoid the amorphous carbon coating.

To confirm that the methane CVD approach produces individual SWNTs, we prepared bulk catalyst supported on alumina nanoparticles. The catalyst preparation involves impregnation of 4.0 g alumina nanoparticles with 1.0 g $Fe(NO_3)_3{\cdot}9H_2O$ in 30 ml methanol for 24 h, after which the methanol is removed by evaporation at 80 °C. Using this bulk catalyst, we carried out methane CVD under exactly the same conditions as with the patterned Si substrates. Using a transmission electron microscope (TEM), we found abundant SWNTs (see Fig. 4 and ref. 17). The diameter range of the individual SWNTs was 1–5 nm, with a mean of 1–2 nm. Ends of SWNTs were frequently observed under TEM. All of the ends imaged so far appear to be closed and free of metal particles (Fig. 4, inset). From these observations, we infer that the SWNTs grow in methane CVD by a 'base-growth' mechanism. Base growth and tip growth are the two mechanisms that have been proposed for CVD growth of various forms of carbon tubes[18–21]. The first step of such a CVD process involves the absorption and decomposition of hydrocarbon molecules on the surface of a transition metal (Fe, Ni, Co, for example) catalyst, followed by diffusion of carbon atoms into the catalyst bulk from the supersaturated surface[19–21]. The tip-growth model involves a metal catalyst particle at a nanotube end being carried away as the nanotube lengthens: thus, the carried-along particle is responsible for supplying carbon feedstock needed for the nanotube growth. In contrast, base growth involves a nanotube lengthening with a particle-free closed end. Carbon feedstock is supplied from the base where the nanotube interfaces with the catalyst material. In our methane CVD system, because there are only closed particle-free nanotube ends we conclude that the base-growth mechanism operates under our conditions. For SWNT syntheses on patterned substrates, we are effectively making catalyst *in situ* in PMMA-defined Petri dishes (Fig. 1). Our synthetic strategy should allow rational design of various single-walled nanotube devices by direct chemical synthesis. □

Received 6 April; accepted 7 July 1998.

1. Thess, A. *et al.* Crystalline ropes of metallic carbon nanotubes. *Science* **273,** 483–487 (1996).
2. Journet, C. *et al.* Large-scale production of single-walled carbon nanotubes by the electric-arc technique. *Nature* **388,** 756–758 (1997).
3. Bethune, D. S. *et al.* Cobalt-catalysed growth of carbon nanotubes with single-atomic-layer walls. *Nature* **363,** 605–607 (1993).
4. Iijima, S. & Ichihashi, T. Single-shell carbon nanotubes of 1-nm diameter. *Nature* **363,** 603–605 (1993).
5. Tans, S. J. *et al.* Individual single-wall carbon nanotubes as quantum wires. *Nature* **386,** 474–477 (1997).
6. Bockrath, M. *et al.* Single-electron transport in ropes of carbon nanotubes. *Science* **275,** 1922–1925 (1997).
7. Odom, T., Huang, J., Kim, P. & Lieber, C. M. Atomic structure and electronic properties of single-walled carbon nanotubes. *Nature* **391,** 62–64 (1998).
8. Wildoer, J. W. G., Venema, L. C., Rinzler, A. G., Smalley, R. E. & Dekker, C. Electronic structure of atomically resolved carbon nanotubes. *Nature* **391,** 59–62 (1997).
9. Kiang, C.-H., Goddard, W. A., Beyers, R., Salem, J. R. & Bethune, D. S. Catalytic synthesis of single-layer carbon nanotubes with a wide range of diameters. *J. Phys. Chem.* **98,** 6612–6618 (1994).
10. Lin, X., Wang, X. K., Dravid, V. P., Chang, R. P. H. & Ketterson, J. B. Large scale synthesis of single-shell carbon nanotubes. *Appl. Phys. Lett.* **64,** 181–183 (1994).
11. Iijima, S. Carbon nanotubes. *MRS Bull.* **19,** 43–49 (1994).
12. Wong, E. W., Sheehan, P. E. & Lieber, C. M. Nanobeam mechanics—elasticity, strength, and toughness of nanorods and nanotubes. *Science* **277,** 1971–1975 (1997).
13. Tibbetts, G. G. in *Carbon Fibers, Filaments and Composites* 73–94 (Kluwer Academic, Amsterdam, 1990).
14. Tibbetts, G. G. Carbon fibers produced by pyrolysis of natural gas in stainless steel tubes. *Appl. Phys. Lett.* **42,** 666–668 (1983).
15. Jaeger, H. & Behrsing, T. The dual nature of vapour-grown carbon fibres. *Composites Sci. Technol.* **51,** 231–242 (1994).
16. Qin, L. C. & Iijima, S. Fibrilliform growth of carbon nanotubes. *Mater. Lett.* **30,** 311–314 (1997).
17. Kong, J., Cassell, A. & Dai, H. Chemical vapor deposition of methane for single-walled carbon nanotubes. *Chem. Phys. Lett.* **292,** 567–574 (1998).
18. Amelinckx, S. *et al.* A formation mechanism for catalytically grown helix-shaped graphite nanotubes. *Science* **265,** 635–639 (1994).
19. Baker, R. T. K. Catalytic growth of carbon filaments. *Carbon* **27,** 315–323 (1989).
20. Tibbetts, G. G., Devour, M. G. & Rodda, E. J. An adsorption-diffusion isotherm and its application to the growth of carbon filaments on iron catalyst particles. *Carbon* **25,** 367–375 (1987).
21. Tibbetts, G. G. Why are carbon filaments tubular? *J. Cryst. Growth* **66,** 632–638 (1984).

Supplementary information is available on *Nature*'s World-Wide Web site (http://www.nature.com) or as paper copy from the London editorial office of *Nature*.

Acknowledgements. We thank J. Brauman, J. Han, C. Marcus, T. Kenny, A. Kapiltulnik and A. Morpurgo for helpful discussions, and J. Kim for his assistance with SEM. This work is partly supported by a Camille and Henry Dreyfus New Faculty Award (H.D.); the NSF and the Office of Naval Research (JSEP) (C.F.Q.); and NASA Ames Research Center (A.M.C.).

Correspondence and requests for materials should be addressed to H.D. (e-mail: hdai@chem.stanford.edu).

Energy implications of future stabilization of atmospheric CO_2 content

Martin I. Hoffert*, Ken Caldeira†, Atul K. Jain‡, Erik F. Haites§, L. D. Danny Harvey‖, Seth D. Potter*¶, Michael E. Schlesinger‡, Stephen H. Schneider#, Robert G. Watts☆, Tom M. L. Wigley & Donald J. Wuebbles‡**

* *Department of Physics, New York University, 4 Washington Place, New York, New York 10003-6621, USA*
† *Lawrence Livermore National Laboratory, Livermore, California 94550, USA*
‡ *Department of Atmospheric Sciences, University of Illinois, Urbana, Illinois 61801, USA*
§ *Margaree Consultants, Toronto, M5H 2X6, Canada*
‖ *Department of Geography, University of Toronto, Toronto, M5S 3G3, Canada*
Department of Biological Sciences, Stanford University, Stanford, Califonia 94305, USA
☆ *Department of Mechanical Engineering, Tulane University, New Orleans, Louisiana 70118, USA*
** *National Center for Atmospheric Research, Boulder, Colorado 80307, USA*

The United Nations Framework Convention on Climate Change[1] calls for "stabilization of greenhouse-gas concentrations in the atmosphere at a level that would prevent dangerous anthropogenic interference with the climate system . . .". A standard baseline scenario[2,3] that assumes no policy intervention to limit greenhouse-gas emissions has 10 TW (10×10^{12} watts) of carbon-emission-free power being produced by the year 2050, equivalent to the power provided by all today's energy sources combined. Here we employ a carbon-cycle/energy model to

¶ Present address: Boeing, Saal Beach, California 90740-7644, USA.